

Invertibility of Multi-Energy X-ray Transform

Yijun Ding^{a)}

*Wyant College of Optical Sciences, University of Arizona, Tucson, AZ,
United States, 85719*

Eric W. Clarkson^{b)}

*Department of Medical Imaging and Wyant College of Optical Sciences,
University of Arizona, Tucson, AZ, United States, 85719*

Amit Ashok^{c)}

*Department of Electrical and Computer Engineering and
Wyant College of Optical Sciences, Tucson, AZ, United States,
85719*

(Dated: 4 May 2022)

Purpose: The goal is to provide a sufficient condition on the invertibility of a multi-energy (ME) X-ray transform. The energy-dependent X-ray attenuation profiles can be represented by a set of coefficients using the Alvarez-Macovski (AM) method. An ME X-ray transform is a mapping from N AM coefficients to N noise-free energy-weighted measurements, where $N \geq 2$.

Methods: We apply a general invertibility theorem which tests whether the Jacobian of the mapping $J(\mathbf{A})$ has zero values over the support of the mapping. The Jacobian of an arbitrary ME X-ray transform is an integration over all spectral measurements. A sufficient condition of $J(\mathbf{A}) \neq 0$ for all \mathbf{A} is that the integrand of $J(\mathbf{A})$ is ≥ 0 (or ≤ 0) everywhere. Note that the trivial case of the integrand equals to zero everywhere is ignored. With symmetry, we simplified the integrand of the Jacobian into three factors that are determined by the total attenuation, the basis functions, and the energy-weighting functions, respectively. The factor related to total attenuation is always positive, hence the invertibility of the X-ray transform can be determined by testing the signs of the other two factors. Furthermore, we use the Cramér-Rao lower bound (CRLB) to characterize the noise-induced estimation uncertainty and provide a maximum-likelihood (ML) estimator.

Results: The factor related to the basis functions is always negative within the energy range normally used for imaging (0–200 keV) when the photoelectric/Compton/Rayleigh basis functions are used and K-edge materials are not considered. The sign of the energy-weighting factor depends on the system source spectra and detector response functions. For four special types of X-ray detectors, the sign of this factor stays the same over the integration volume. Therefore, when these four types of detectors are used for imaging non-K-edge materials, the ME X-ray transform is globally invertible. The same framework can be used to study an arbitrary ME X-ray imaging system. Furthermore, the ML estimator we presented is an unbiased, efficient estimator and can be used for a wide range of scenes.

Conclusions: We have provided a framework to study the invertibility of an arbitrary ME X-ray transform and proved the global invertibility for four types of systems.

Keywords: invertibility, X-ray, multi-energy X-ray imaging, spectral X-ray imaging

I. INTRODUCTION

Muti-energy (ME) X-ray imaging, also called spectral or energy-selective X-ray imaging, has long been used to image the chemical composition of the object being scanned¹⁻⁶. In X-ray imaging, the chemical composition of a material is characterized by the energy dependence of the X-ray attenuation profile. Since an X-ray attenuation profile is a linear combination of basis functions with known energy dependences, it can be summarized by a few energy-independent coefficients as in the Alvarez-Macovski method¹. We will call these coefficients the AM coefficients. Imaging the AM coefficients requires multiple energy-weighted measurements, e.g. energy integration with varying source tube voltages or photo-counting with multiple bins. We refer to the mapping from the AM coefficients to the energy-weighted measurements an X-ray transform. The question whether an X-ray transform is invertible or not has only been explored for dual-energy (DE) measurements^{7,8}. The purpose of this paper is to provide a sufficient condition on the invertibility of a general ME X-ray transform.

With the recent development in ME X-ray detectors, DE X-ray imaging is becoming obsolete. DE X-ray imaging recovers two AM coefficients¹ that specify the amount of contribution from photoelectric effect and Compton scattering to the linear attenuation profile, respectively. The contribution from Rayleigh scattering has been considered negligible or assumed to be captured by the other two AM coefficients in DE X-ray imaging⁹⁻¹¹. However, it is hard to predict the effect caused by ignoring the Rayleigh scattering term due to the nonlinear nature of the X-ray transform, especially for security- and industrial-screening applications where the materials of interest are not necessarily low-Z materials. With ME detectors, the AM coefficient corresponding to the Rayleigh scattering can be recovered. Furthermore, ME X-ray imaging systems can image materials containing K-edges in the spectral range used for imaging⁵.

With broad-spectrum X-ray sources, measurements of many X-ray systems are naturally energy-weighted¹². ME measurements can be acquired with varying source settings^{13,14} or with a detector that registers multiple signals, such as sandwich detectors¹⁵, counting and integrating X-ray (CIX) detectors¹⁶ and multi-bin photon-counting detectors¹⁷. More specifically, the recent advancement in photon counting detectors with pulse height analysis, which can output in multiple energy levels, provides a paradigm shift in X-ray detector

technology and is enabling many new applications¹⁸.

The invertibility of a transform is a fundamental question in inverse problems. An invertibility problem considers noise-free measurements and determines whether a unique solution exists. A system of N linear equations of N unknowns has a unique solution (as long as the forward matrix is invertible); this is not necessarily true for nonlinear transforms. Levine et. al.⁷ has demonstrated a case of DE X-ray imaging with non-unique solutions. Alvarez et. al.⁸ has applied an inverse function theorem for two-dimensional transforms¹⁹ to a DE X-ray transform. With the inclusion of Rayleigh scattering and/or the presence of K-edge materials, more AM coefficients and hence ME measurements are required. The invertibility of an ME X-ray transform is not an obvious extension of the DE X-ray transform.

In this paper, we provide a framework to study the invertibility of an arbitrary ME X-ray transform and proved the invertibility for four special cases of energy-weighted detectors. Furthermore, we consider Poisson noise in the measurement data and present the Cramér-Rao lower bound (CRLB) on the estimation of AM coefficients. Lastly, we provide a fast maximum-likelihood (ML) algorithm for coefficients estimation and demonstrate the application of this algorithm in reconstruction.

II. ME X-RAY TRANSFORM

In the energy range commonly used for X-ray transmission imaging, the interaction between X-ray photons and the medium can be categorized into the following three processes: photoelectric absorption, Compton scattering and coherent (Rayleigh) scattering. Correspondingly, the X-ray linear attenuation coefficient profiles can be represented accurately by a summation of N terms as:

$$\mu(E) = \sum_i^N a_i f_i(E) = \mathbf{a} \cdot \mathbf{f}(E), \quad (1)$$

where each component of \mathbf{f} is a function of energy E , the coefficients \mathbf{a} are determined by the material composition, and the N terms include photo electric, Compton scattering, Rayleigh scattering and K-edges. Here 'photo electric' refers to the smooth energy dependence of the photo electric effect and 'K-edges' refer to the discontinuities in the energy dependence of the photo electric effect. We use this set of $f_i(E)$ functions as basis functions and the coefficients \mathbf{a} as the AM coefficients.

For materials that do not contain K-edges in the energy range of interest, the number of basis functions needed is $N = 3$. Approximated expressions of photo electric and Rayleigh scattering term have been provided in Williamson et al.²⁰ by fitting to DLC-146 cross-section data²¹ and the Klein-Nishina function¹ describes the Compton scattering term:

$$\begin{cases} f_1(E) = c_1 E^{-3.088}, \\ f_2(E) = c_2 \left(\frac{1 + \alpha}{\alpha^2} \left[\frac{2(1 + \alpha)}{1 + 2\alpha} - \frac{1}{\alpha} \ln(1 + 2\alpha) \right] + \frac{1}{2\alpha} \ln(1 + 2\alpha) - \frac{1 + 3\alpha}{(1 + 2\alpha)^2} \right), \\ f_3(E) = c_3 E^{-1.737}, \end{cases} \quad (2)$$

where $\alpha = E/(510.975 \text{ keV})$, the subscript 1,2,3 refers to the photoelectric effect, the Compton scattering and the Rayleigh scattering, and c_i are normalization factors so that $\|f_i(E)\|_2 = 1$. The normalized basis functions are presented in Figure 1 (left). The usefulness of these functions in representing attenuation coefficient profiles is well known. We generated attenuation profiles for 128 materials based on the NIST XCOM data²². Example of materials include Delrin, water, soap and cast magnesium. For each material, 1000 samples of slight different material compositions were generated. These attenuation profiles (K-edge materials excluded) were fitted by the three functions using a least-squares curve-fitting routine. Over the range of 20–200 keV, the largest difference between the fitted value and the XCOM value was less than 2.5% with an average error of 0.66%. As an example, the fitted attenuation profile and the XCOM data for water are presented in Figure 1 (right).

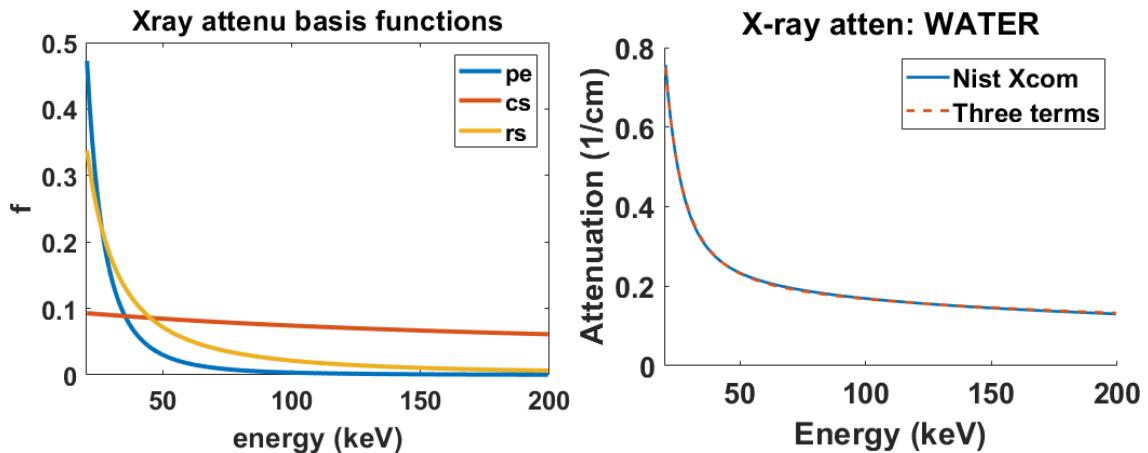


FIG. 1: Shape of $f_i(E)$ for $i = 1, 2, 3$ (left) and fitted attenuation profile of water (right).

The total attenuation $\tau_{\theta,\rho}(E)$ is the line integral of the X-ray attenuation coefficient

$\mu(\mathbf{R}, E)$ along the ray path with rotation angle θ and position along the detector plane ρ :

$$\tau_{\theta,\rho}(E) = \int_{\theta,\rho} dl \mu(\mathbf{R}, E) = \sum_{i=1}^N A_i(\theta, \rho) f_i(E) = \mathbf{A}(\theta, \rho) \cdot \mathbf{f}(E), \quad (3)$$

where

$$A_i(\theta, \rho) = \int_{\theta,\rho} dl a_i(\mathbf{R}) \quad (4)$$

is a sinogram of the i^{th} AM coefficient. For a pencil-beam system, $A_i(\theta, \rho)$ is the Radon transform of $a_i(\mathbf{R})$.

The object $a_i(\mathbf{R})$ can be reconstructed from the sinograms $A_i(\theta, \rho)$, and the line integrals $A_i(\theta, \rho)$ can be estimated from ME measurements of the corresponding ray path. For a given ray path, the mean signal of the m^{th} measurement can be described by

$$\begin{aligned} I_m &= I_0 \int_0^\infty dE D_m(E) S_m(E) \exp[-\mathbf{A} \cdot \mathbf{f}(E)] \\ &= I_0 \int_0^\infty dE p_m(E) \exp[-\mathbf{A} \cdot \mathbf{f}(E)] \end{aligned} \quad (5)$$

where $m = 1, \dots, M$, I_0 is the source photon budget, $D_m(E)$ is the detector response of the m^{th} measurement, $S_m(E)$ is the normalized source spectrum of the m^{th} measurement, and $p_m(E) = D_m(E)S_m(E)$ is the combined energy-weighting function. This equation can be used to describe many energy-weighted measurements, such as a photon-counting (PC) binning detector and an energy-integrating detector. In the most general case, the source spectra may vary across measurements and the combined weighting functions are arbitrary and can take on any real non-negative values at each energy.

A special case of a ME detector is a CIX detector that counts the number of photons and integrates both the energy and the momentum of the photons (PC/EI/MI), providing measurements with detector response $D_1(E) = 1$, $D_2(E) \propto E$ and $D_3(E) \propto \sqrt{E}$ as shown in Figure 2(a). Since a CIX PC/EI detector has been developed¹⁶, it is reasonable to assume that building a CIX PC/EI/MI detector is feasible. A second special case is a binning detector where the weighting functions are arbitrary and non-overlapping as shown in Figure 2(b). Another special case is an ideal PC detector as illustrated in Figure 2(c), where the detector response of each bin can be considered as *rect* functions and there may be overlaps between different bins. Binning detectors in real life tend to have non-overlapping bins.

Here, for the comprehensiveness, we include detectors with overlap bins. Another special case considers the finite energy resolution in a non-overlapping three-bin rect detector. The detector response functions of such a detector are plotted in Figure 2(d).

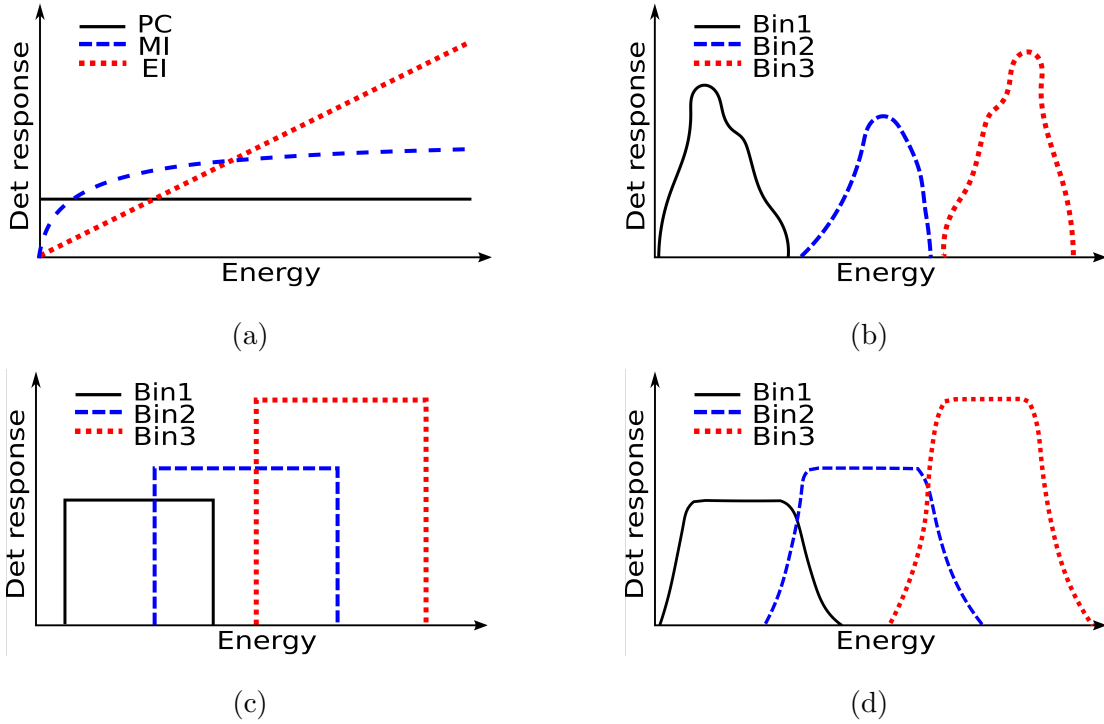


FIG. 2: Energy weighting functions for four special cases: (a) CIX-PC/EI/MI, (b) non-overlapping bins with arbitrary response, (c) three *rect* bins with ideal energy resolution, and (d) three non-overlapping *rect* bins with finite energy resolution.

III. INVERTIBILITY

In this section, we explore the invertibility of the mapping from the AM coefficients \mathbf{A} to the noise-free ME measurement data \mathbf{I} . Suppose we have $M = N$ measurements. The coefficients \mathbf{A} and the mean photon count \mathbf{I} are both in N -dimensional Euclidean space \mathbf{R}^N .

III.A. Inequalities

We derive the bounds on the coefficients \mathbf{A} for given measurement data \mathbf{I} . Using Jensen's inequality, we have

$$\ln \frac{I_m}{d_m I_0} > \int_0^\infty dE \frac{p_m(E)}{d_m} [-\mathbf{A} \cdot \mathbf{f}(E)], \quad (6)$$

where d_m is a normalization factor, which equals to $\int_0^\infty dE p_m(E)$. These inequalities can be written as

$$\mathbf{A} \cdot \mathbf{n}_m > -\ln[I_m/(d_m I_0)] \quad (7)$$

where

$$\mathbf{n}_m = \int_0^\infty dE p_m(E) \mathbf{f}(E) / d_m \quad (8)$$

The vector \mathbf{n}_m has all non-negative components. Furthermore, the mean photon count after the attenuation, I_m , is always less than or equal to the mean source photon count, $d_m I_0$. Therefore, the right hand side of Equation (7) is always larger than or equal to 0. Each of the inequalities in Equation (7) forces the vector \mathbf{A} to be on the side that is opposite to the origin of the hyperplane defined by $\mathbf{A} \cdot \mathbf{n}_m = -\ln[I_m/(d_m I_0)]$, as shown in Figure 3a for the case of $N = 2$.

From the Schwarz inequality we have

$$I_m^2 < I_0^2 \left[\int_{S_m} dE p_m^2(E) \right] \left[\int_{S_m} dE \exp[-2\mathbf{A} \cdot \mathbf{f}(E)] \right]. \quad (9)$$

If we define

$$\gamma_m = \frac{I_m^2}{I_0^2} \left[\int_{S_m} dE p_m^2(E) \right]^{-1}, \quad (10)$$

then we have

$$\gamma_m < \int_{S_m} dE \exp[-2\mathbf{A} \cdot \mathbf{f}(E)]. \quad (11)$$

We define the support of the weighting functions $p_m(E)$ as S_m and assume that the length $|S_m|$ of each support set is finite. Replacing the integrand with its maximum possible value gives

$$\gamma_m < \exp \left\{ -2 \min_{E \in S_m} [\mathbf{A} \cdot \mathbf{f}(E)] \right\} |S_m| \quad (12)$$

Note that, since $\mathbf{A} \cdot \mathbf{f}(E) > 0$, this inequality implies that $\gamma_m < |S_m|$. Therefore we have another set of inequalities

$$\min_{E \in S_m} [\mathbf{A} \cdot \mathbf{f}(E)] < \frac{1}{2} \ln \left(\frac{|S_m|}{\gamma_m} \right) \quad (13)$$

Now we may choose an energy E_m such that

$$\mathbf{A} \cdot \mathbf{f}(E_m) < \frac{1}{2} \ln \left(\frac{|S_m|}{\gamma_m} \right) \quad (14)$$

Each of these inequalities forces the vector \mathbf{A} to be on the same side of the corresponding
100 hyperplane as the origin.

Since the vector \mathbf{A} is non-negative, for given mean photon count \mathbf{I} , these inequalities force \mathbf{A} to be in a closed and bounded set defined by the first set of hyperplanes, the second set of hyperplanes, and the coordinate hyperplanes defined by $A_i = 0$. A typical picture of this situation for $N = 2$ is shown in Figure 3a.

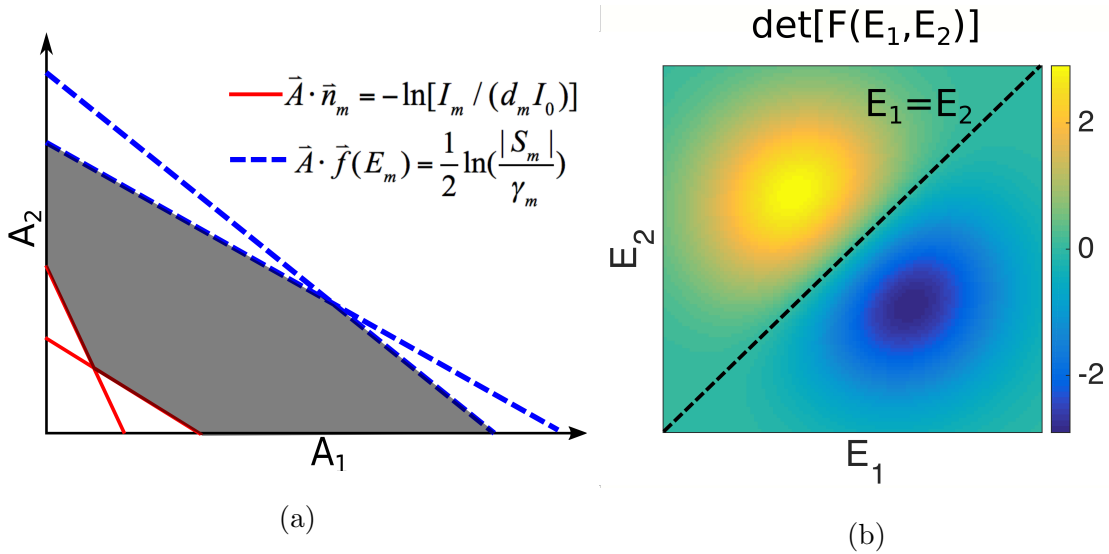


FIG. 3: (a) For given noise-free measurement data \mathbf{I} , the vector \mathbf{A} is bounded in the area indicated in grey. (b) Illustration of the sign-switched mirror symmetry in function

$$\det[F(E_1, E_2)] \text{ along line } E_1 = E_2.$$

III.B. Jacobian

The first-order and second-order derivatives of the X-ray transform are as follows:

$$\begin{aligned}\frac{\partial I_m}{\partial A_i} &= -I_0 \int_0^\infty dE p_m(E) f_i(E) \exp[-\mathbf{A} \cdot \mathbf{f}(E)], \\ \frac{\partial^2 I_m}{\partial A_i \partial A_j} &= I_0 \int_0^\infty dE p_m(E) f_i(E) f_j(E) \exp[-\mathbf{A} \cdot \mathbf{f}(E)].\end{aligned}\tag{15}$$

The second-order derivative exists and is continuous, therefore the mapping $\mathcal{X} : \mathbf{A} \rightarrow \mathbf{I}$ is a C^2 mapping.

The values $\mathbf{I}(0)$, which represents the mean signals of an air scan, are finite. Therefore, the mapping \mathcal{X} can be easily modified into $\mathcal{X}' : \mathbf{a} \rightarrow \mathbf{I} - \mathbf{I}(0)$ to satisfy $\mathcal{X}'(0) = 0$. This subtraction of a constant does not change the first and second derivatives of the mapping.

The Jacobian of the mapping is $J(\mathbf{A}) = |\det(\nabla_{\mathbf{A}} \mathbf{I})|$, where $|\cdot|$ represents the absolute value and $\det(\cdot)$ is the determinant of a matrix. Define the set $S = S_1 \times S_2 \dots \times S_M$, we can write the determinant as:

$$\begin{aligned}\det(\nabla_{\mathbf{A}} \mathbf{I}) &= (-I_0)^M \int_S d^M \mathbf{E} \left\{ \prod_{m=1}^M p_m(E_m) e^{-\mathbf{A} \cdot \mathbf{f}(E_m)} \right\} \det[F(\mathbf{E})], \\ &= (-I_0)^M \int_S d^M \mathbf{E} \left\{ \prod_{m=1}^M f_m(E_m) e^{-\mathbf{A} \cdot \mathbf{f}(E_m)} \right\} \det[P(\mathbf{E})],\end{aligned}\tag{16}$$

where the matrix F as a function of $\mathbf{E} = (E_1, E_2, \dots, E_M)$ is

$$F(\mathbf{E}) = \begin{bmatrix} f_1(E_1) & f_2(E_1) & \dots & f_N(E_1) \\ f_1(E_2) & f_2(E_2) & \dots & f_N(E_2) \\ \dots & \dots & \dots & \dots \\ f_1(E_M) & f_2(E_M) & \dots & f_N(E_M) \end{bmatrix},\tag{17}$$

and the matrix P as a function of \mathbf{E} is

$$P(\mathbf{E}) = \begin{bmatrix} p_1(E_1) & p_2(E_1) & \dots & p_N(E_1) \\ p_1(E_2) & p_2(E_2) & \dots & p_N(E_2) \\ \dots & \dots & \dots & \dots \\ p_1(E_M) & p_2(E_M) & \dots & p_N(E_M) \end{bmatrix}.\tag{18}$$

The integrand in Equation (16) has interesting symmetry properties. The factor $\prod_{m=1}^M e^{-\mathbf{A} \cdot \mathbf{f}(E_m)} = e^{-\mathbf{A} \cdot \sum_{m=1}^M \mathbf{f}(E_m)}$ has mirror symmetry about all hyperplanes $E_i = E_j$

for $i, j \in \{1, 2, \dots, M\}$. The other factor, $\det[F(\mathbf{E})]$, has sign-switching mirror symmetry about the same hyperplanes, which can be described mathematically as:

$$\det[F(E_1, E_2, \dots, E_M)] = \text{sgn}(\boldsymbol{\sigma}) \det[F(E_{\sigma_1}, E_{\sigma_2}, \dots, E_{\sigma_M})]. \quad (19)$$

where the sign of the permutation $\boldsymbol{\sigma}$, $\text{sgn}(\boldsymbol{\sigma})$, is +1 or -1 for even or odd permutation, respectively. A sign-switching mirror symmetry means that, when we switch the positions of two coordinates (odd permutation), the sign of the function changes but the absolute value of the function is preserved. For example, with two coordinates E_1 and E_2 , $\det[F(E_1, E_2)] = f_1(E_1)f_2(E_2) - f_2(E_1)f_1(E_2) = -\det[F(E_2, E_1)]$. To illustrate the sign-switching mirror symmetry, we plotted $\det[F(E_1, E_2)]$ for the case when $f_1(E)$ and $f_2(E)$ are both Gaussian functions in Figure 3b.

Now we can divide the space occupied by S into $M!$ subspaces with hyperplanes $E_i = E_j$ for $i, j \in \{1, 2, \dots, M\}$. One of the subspace has property $E_1 < E_2 < \dots < E_M$ and we define this subspace as $S_{12\dots M}$. For every point (E_1, E_2, \dots, E_M) in the subspace $S_{12\dots M}$, there is a corresponding point $(E_{\sigma_1}, E_{\sigma_2}, \dots, E_{\sigma_M})$ in each of the remaining subspaces. Applying the sign-switching mirror symmetry of the determinant, we can further simplify the Jacobian to:

$$\begin{aligned} \det(\nabla_{\mathbf{A}} \mathbf{I}) &= (-I_0)^M \int_{S_{12\dots M}} d^M \mathbf{E} \left\{ \prod_{m=1}^M e^{-\mathbf{A} \cdot \mathbf{f}(E_m)} \right\} \det[F(\mathbf{E})] \sum_{\boldsymbol{\sigma}} \text{sgn}(\boldsymbol{\sigma}) \prod_{m=1}^M p_m(E_{\sigma_m}), \\ &= (-I_0)^M \int_{S_{12\dots M}} d^M \mathbf{E} \left\{ \prod_{m=1}^M e^{-\mathbf{A} \cdot \mathbf{f}(E_m)} \right\} \det[F(\mathbf{E})] \det[P(\mathbf{E})]. \end{aligned} \quad (20)$$

Note that we consider systems with $M = N$. The symbol M is used here to emphasize the integration is over all spectral measurements. The three factors of the integrand, $\prod_{m=1}^M e^{-\mathbf{A} \cdot \mathbf{f}(E_m)}$, $\det[F(\mathbf{E})]$ and $\det[P(\mathbf{E})]$ depend on the total attenuation, the basis functions and the energy-weighting functions, respectively.

III.C. Proper

Now we show that the mapping $\mathcal{X} : \mathbf{A} \rightarrow \mathbf{I}$ is a proper mapping. If we have a compact set C in the hypercube in data space, where all of the data vectors are located, then there are maximum and minimum values for each I_m over all \mathbf{I} in C . The maximum value for

I_m determines the hyperplane $\mathbf{A} \cdot \mathbf{n}_m = -\ln[I_m/(d_m I_0)]$ that is closet to the origin. The minimum value for I_m determines the hyperplane

$$\mathbf{A} \cdot \mathbf{f}(E_m) = \frac{1}{2} \ln \left(\frac{|S_m|}{\gamma_m} \right) \quad (21)$$

that is furthest away from the origin. Therefore, the set of \mathbf{A} that are mapped into C are contained in a region bounded by these hyperplanes and the coordinate hyperplanes. This is a closed and bounded set in \mathbb{R}^N , hence a compact set. Since the map $\mathbf{I}(\mathbf{A})$ is continuous, the set of \mathbf{A} that are mapped into the closed set C is closed. The set of \mathbf{A} that are mapped into C is a closed subset of a compact set. This set is therefore also compact. As a result, the mapping $\mathbf{I}(\mathbf{A})$ is proper.

III.D. Invertibility

130 **The Hadamard's global inverse function theorem**²³: *Let $\mathcal{X} : \mathbf{R}^N \rightarrow \mathbf{R}^N$ be a C^2 mapping. Suppose that $\mathcal{X}(0) = 0$ and that the Jacobian determinant of \mathcal{X} is nonzero at each point. Further suppose that \mathcal{X} is proper. Then \mathcal{X} is one-to-one and onto.*

The mapping $\mathcal{X} : \mathbf{A} \rightarrow \mathbf{I}$ has satisfied all requirements to be globally invertible except one: the Jacobian determinant is nonzero for all \mathbf{A} in the support. A sufficient but not necessary condition for $J(\mathbf{A}) \neq 0$ is that the integrand of $J(\mathbf{A})$ given in Equation (20) has the same sign over the subspace $S_{12\dots N}$ and is not zero in some region. The first factor in the integrand, which depends solely on the total attenuation, is always positive. Therefore, a sufficient condition for the invertibility of the ME X-ray transform is $\det[F(\mathbf{E})] \det[P(\mathbf{E})] \leq 0$ (or ≥ 0) over the entire subspace $S_{12\dots N}$. Throughout the paper, we ignore the trivial case 140 that $\det[F(\mathbf{E})] \det[P(\mathbf{E})] = 0$ everywhere.

The basis-function determinant $\det[F(\mathbf{E})]$ is always negative in the subspace S_{123} when the photoelectric/Compton/Rayleigh basis functions are used. These three basis functions are sufficient to describe the scene when the materials of interest have no K-edges in the energy range normally used for imaging (0–200 keV), e.g. soft tissue and bone. The proof of $\det[F(\mathbf{E})] < 0$ for all \mathbf{E} that satisfy $0 < E_1 < E_2 < E_3 < 200$ keV is provided in Appendix A. When K-edge materials are considered, the values of $\det[F(\mathbf{E})]$ can be calculated numerically and the positive regions of $\det[F(\mathbf{E})]$ can be avoided by adjusting the detector sensitivity or source spectrum in $p_m(E)$.

We then consider the sign of $\det[P(\mathbf{E})]$ for the four types of detectors illustrated in Figure 2. Assuming the source spectrum $S(E)$ is same for different m , the weighting-function determinant $\det[P(\mathbf{E})]$ has the same sign with the detector-response determinant $\det[D(\mathbf{E})]$, where the (i, j) element of matrix $D(\mathbf{E})$ is the detector response of the i^{th} measurement at E_j denoted as $D_i(E_j)$. We consider the sign of $\det[D(\mathbf{E})]$ for the four types of detectors.

- (a). An CIX-PC/EI/MI detector: $\det[D(\mathbf{E})] < 0$ for all $\mathbf{E} \in S_{123}$.
- (b). A three bin detector, where the three bins are not overlapping and the energy-response functions are arbitrary: $\det[D(\mathbf{E})] \geq 0$ for all $\mathbf{E} \in S_{123}$.
- (c). A three bin PC detector with *rect*-response functions and possible overlaps between bins: if Bin 1 and Bin 3 has no overlap, the lower edges of the three bins satisfy $l_1 < l_2 < l_3$ and the upper edges of the three bins satisfy $u_1 < u_2 < u_3$, the determinant $\det[D(\mathbf{E})] \geq 0$ for all $\mathbf{E} \in S_{123}$.
- (d). A non-overlapping three bin PC detector with finite energy resolution: if the energy resolution of the detector can be modeled by a narrow truncated function (for mathematical description see Appendix A) and there is no overlap between Bin 1 and Bin 3, $\det[D(\mathbf{E})] \geq 0$ in S_{123} .

Detailed proofs are provided in Appendix A. In conclusion, the mapping $\mathcal{X} : \mathbf{A} \rightarrow \mathbf{I}$ is globally invertible for these four types of detectors when measuring attenuation profiles without K-edges. For arbitrary detectors or systems with varying source spectra, the values of $\det[P(\mathbf{E})]$ can be calculated numerically. One can always maintain $\det[F(\mathbf{E})] \det[P(\mathbf{E})] \leq 0$ for any E in $S_{12\dots N}$ by adjusting the energy-response function or the bin boundaries of the detectors.

IV. ESTIMATION UNCERTAINTIES FOR POISSON DATA

Invertibility does not necessary mean estimability. It is also crucial to consider the uncertainty in the estimation under the presence of noise. In this section, we consider PC detectors with non-overlapping bins. If only inherent quantum noise is considered, the data of the m^{th} measurement at a given ray path, g_m , is a Poisson random variable with mean

equals to I_m ,

$$g_m(\mathbf{A}) = \mathcal{P}oiss(I_m(\mathbf{A})), \quad (22)$$

where $I_m(\mathbf{A})$ is the mean photon count of the m^{th} measurement given in Equation (5). Combine all M measurements, we get the measurement data \mathbf{g} . The probability density function of the data \mathbf{g} given the AM coefficient \mathbf{A} along the ray path is

$$\text{pr}(\mathbf{g}|\mathbf{A}) = \prod_{m=1}^M \frac{I_m(\mathbf{A})^{g_m} e^{-I_m(\mathbf{A})}}{g_m!} \quad (23)$$

The log-likelihood function of the AM coefficients \mathbf{A} is

$$L(\mathbf{A}|\mathbf{g}) = \ln \text{pr}(\mathbf{g}|\mathbf{A}) = \sum_{m=1}^M g_m \ln I_m(\mathbf{A}) - I_m(\mathbf{A}) - \ln g_m!. \quad (24)$$

The first derivative of the log-likelihood function is

$$\frac{\partial L}{\partial A_i}(\mathbf{A}) = \sum_{m=1}^M \frac{g_m - I_m(\mathbf{A})}{I_m(\mathbf{A})} \frac{\partial I_m}{\partial A_i}(\mathbf{A}) = \sum_{m=1}^M \frac{g_m - I_m(\mathbf{A})}{I_m(\mathbf{A})} [\nabla_{\mathbf{A}} \mathbf{I}]_{mi}. \quad (25)$$

The Hessian, or second derivative, of the log-likelihood function is given by

$$[\nabla_{\mathbf{A}}^2 L]_{ij} = \frac{\partial^2 L}{\partial A_i \partial A_j} = \sum_{m=1}^M \frac{g_m - I_m}{I_m} \frac{\partial^2 I_m}{\partial A_i \partial A_j} - \frac{g_m}{I_m^2} \frac{\partial I_m}{\partial A_i} \frac{\partial I_m}{\partial A_j}. \quad (26)$$

The components of the Fisher information matrix are

$$\begin{aligned} F_{ij}(\mathbf{A}) &= - \left\langle \frac{\partial^2 L}{\partial A_i \partial A_j} \right\rangle_{\mathbf{g}|\mathbf{A}} \\ &= - \int d^M \mathbf{g} \text{pr}(\mathbf{g}|\mathbf{A}) \sum_{m=1}^M \left[\frac{g_m - I_m}{I_m} \frac{\partial^2 I_m}{\partial A_i \partial A_j} - \frac{\partial I_m}{\partial A_i} \frac{\partial I_m}{\partial A_j} \frac{g_m}{I_m^2} \right] \\ &= \sum_{m=1}^M \frac{1}{I_m} \frac{\partial I_m}{\partial A_i} \frac{\partial I_m}{\partial A_j}. \end{aligned} \quad (27)$$

Therefore, the Fisher information matrix is

$$F(\mathbf{A}) = (\nabla_{\mathbf{A}} \mathbf{I})^T \Lambda^{-1} (\nabla_{\mathbf{A}} \mathbf{I}), \quad (28)$$

where Λ is a diagonal matrix with the m^{th} diagonal element equals to I_m .

The *Crámer-Rao bounds*^{24,25} characterize the limit on the estimation uncertainties induced by noise. It states that the unbiased estimate of the i^{th} parameter has a variance that must

be at least as large as the i^{th} diagonal element of the inverse of the Fisher information matrix. Mathematically, the Crámer-Rao lower bounds are

$$\text{Var}(\hat{A}_i - A_i) \geq [F^{-1}]_{ii} = [(\nabla_{\mathbf{A}}\mathbf{I})^{-1}\Lambda(\nabla_{\mathbf{A}}\mathbf{I})^{-1,T}]_{ii}, \quad (29)$$

where the symbol \hat{A} indicates an estimate of A . Note that the uncertainty in the estimation is inversely related with the source photon budget I_0 , which agrees with our intuition. Also Note that the uncertainty of an unbiased estimation is inversely related with the Jacobian $J(\mathbf{A}) = |\det(\nabla_{\mathbf{A}}\mathbf{I})|$. If the Jacobian $J(\mathbf{A})$ is close to zero, the estimation uncertainty is close to infinity and the coefficients are practically not estimable.

V. ESTIMATION ALGORITHM AND ILLUSTRATIVE RESULTS

To estimate \mathbf{A} from data \mathbf{g} , we develop an ML estimation algorithm. First, consider L as a function of mean signal \mathbf{I} . The first derivation of this function is

$$\frac{\partial L}{\partial I_i} = \frac{g_i}{I_i} - 1. \quad (30)$$

Hence, the point $\mathbf{I} = \mathbf{g}$ is a critical point. The Hessian of the function $L(\mathbf{I}|\mathbf{g})$ is

$$[\nabla_{\mathbf{I}}^2 L]_{ij} = \frac{\partial^2 L}{\partial I_i \partial I_j} = -\frac{g_i}{I_i^2} \sigma_{ij} \quad (31)$$

where $\sigma_{ij} = 1$ when $i = j$, and $\sigma_{ij} = 0$ otherwise. This Hessian is a diagonal matrix with all
180 negative elements when $g_m > 0$. Therefore, the function $L(\mathbf{I}|\mathbf{g})$ is a concave function and the critical point at $\mathbf{I} = \mathbf{g}$ is the global maximum for L . When the mapping $\mathcal{X} : \mathbf{A} \rightarrow \mathbf{I}$ is invertible and \mathbf{g} is within the range of the mapping, the maximum value of L corresponds to a point \mathbf{A}_g that satisfies $\mathbf{I}(\mathbf{A}_g) = \mathbf{g}$.

We then consider L as function of the AM coefficients \mathbf{A} . When the matrix $\nabla_{\mathbf{A}}\mathbf{I}$ is invertible, which is true when the X-ray transform is invertible, the likelihood function $L(\mathbf{A}|\mathbf{g})$ has only one critical point and this point is \mathbf{A}_g , which has the maximum likelihood. An ML algorithm can be developed based on Newton's method^{26,27} with iterations described as

$$\mathbf{A}_{k+1} = \mathbf{A}_k + t_k * \Delta \mathbf{A}_k, \quad \text{and} \quad \Delta \mathbf{A}_k = -[\nabla_{\mathbf{A}}^2 L(\mathbf{A}_k)]^{-1} \nabla_{\mathbf{A}} L(\mathbf{A}_k), \quad (32)$$

where \mathbf{A}_k is the attenuation coefficients at iteration k and t_k is the step size chosen with an Armijo-type (or back-tracking) line search to enforce sufficient increase in L and the

negativeness of the Hessian $\nabla_{\mathbf{A}}^2 L$. Note this algorithm only works when there are no zero counts in any bins.

V.A. Estimation uncertainties

To demonstrate the applications of this ML algorithm, we considered an ideal three-bin
 190 PC detector with non-overlapping *rect* response functions and a broad spectrum X-ray source
 operated at 160 kVp²⁸. The data were simulated at source photon budget $I_0 = 10^7$ with
 Poisson noise.

We simulated a single X-ray path with different lengths of water as the attenuation
 media. The detector energy bin boundaries were set at [30, 75, 100, 160] keV. The length of
 water ranged from 1 cm to 28 cm. For each length, 1000 sets of noisy data were generated,
 and the AM coefficients were estimated for each set of data. We calculated the mean and
 the variance of the estimated coefficients and compared the estimation uncertainty to the
 Crámer-Rao lower bound. The results are presented in Figure 4.

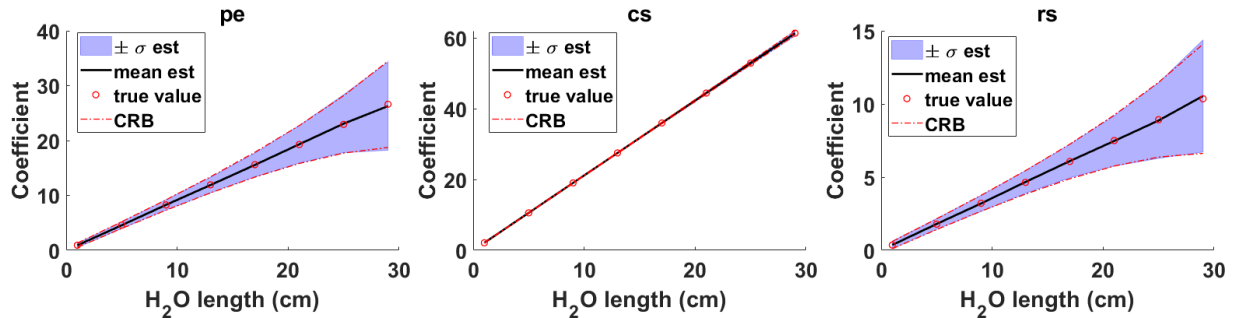


FIG. 4: Uncertainties in the three estimated pe/cs/rs coefficients for different lengths of
 water.

To check if the algorithm works for materials that are very different from water, we
 200 changed the material in the X-ray path to iron and the detector bin boundaries to [30,
 110, 140, 160] keV. The bin boundaries were changed so that there are sufficient number of
 photons collected in all bins. The length of iron ranged from 0.1 cm to 3 cm. The mean and
 variance of the 1000 estimations at each length are presented in Figure 5.

In both scenarios, the mean of the estimates (black line) matches well with the true
 coefficient (red circle). The slight deviation between the true coefficient and the mean
 estimation at high attenuation region can be explained by sampling error in Monte-Carlo

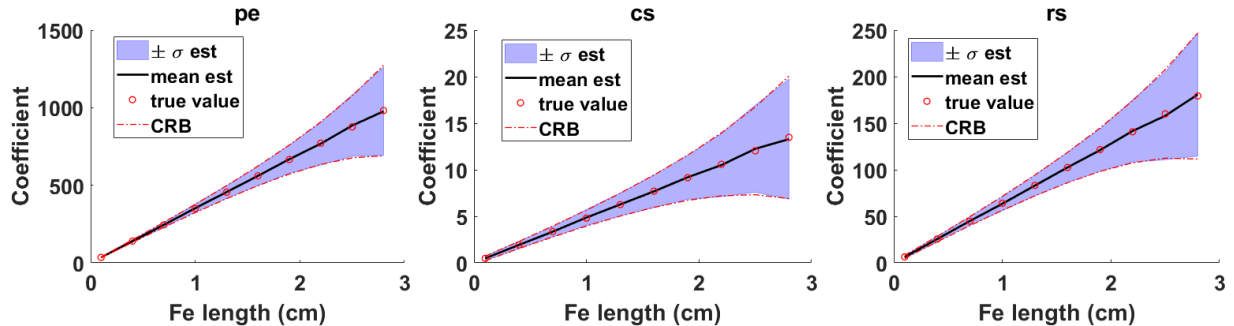


FIG. 5: Uncertainties in the estimated pe/cs/rs coefficients for different lengths of iron.

simulation. The standard deviation of the estimates (purple area) is almost perfectly aligned with the Crámer-Rao lower bound. These results show that our estimation algorithm is unbiased and efficient. Furthermore, the AM coefficient corresponding to the Rayleigh scattering is estimable and the uncertainty in \hat{A}_{rs} is comparable to the uncertainty in \hat{A}_{pe} , which corresponds to the photoelectric effect.

V.B. Phantom reconstruction

We further applied the ML estimation algorithm in reconstruction. The reconstruction problem in X-ray computed tomography (CT) is to estimate the distribution $\mathbf{a}(\mathbf{R})$ from the estimated line integrals $\hat{\mathbf{A}}$ for each ray path. The AM coefficients \mathbf{a} at each location \mathbf{R} correspond to an attenuation profile $\mu(E)$. For a two-dimensional scene, the object $\mu(E, \mathbf{R})$ and the reconstruction $\hat{\mu}(E, \mathbf{R})$ are both three-dimensional data cubes. To present the reconstruction result, we plot $\mu(E, \mathbf{R})$ and $\hat{\mu}(E, \mathbf{R})$ at an arbitrary energy.

We simulated a two-dimensional fan-beam CT system with 360 views and 245 detectors spanning 61.25° per view. The field of view is 256x256 pixels with pixel pitch 0.1–0.15 cm. The same source and the same detector mentioned in the previous section were used. The detector energy bin boundaries were [30, 75, 100, 160] keV. The source photon budget for each beam path was 10^7 . The AM coefficients \mathbf{A} were estimated for each beam path and the object represented by $\mathbf{a}(\mathbf{R})$ was reconstructed from $\hat{\mathbf{A}}$ with filtered-back projection (FBP).

The first phantom reconstructed is a circular water phantom of diameter about 30 cm with pixel-pitch 0.15 cm. This phantom and its reconstruction are plotted at $E = 75.5$ keV in Figure 6. The reconstruction matches well with the object. As shown in the center-line plot in the right panel of Figure 6, the reconstruction has no cupping artifacts, which is

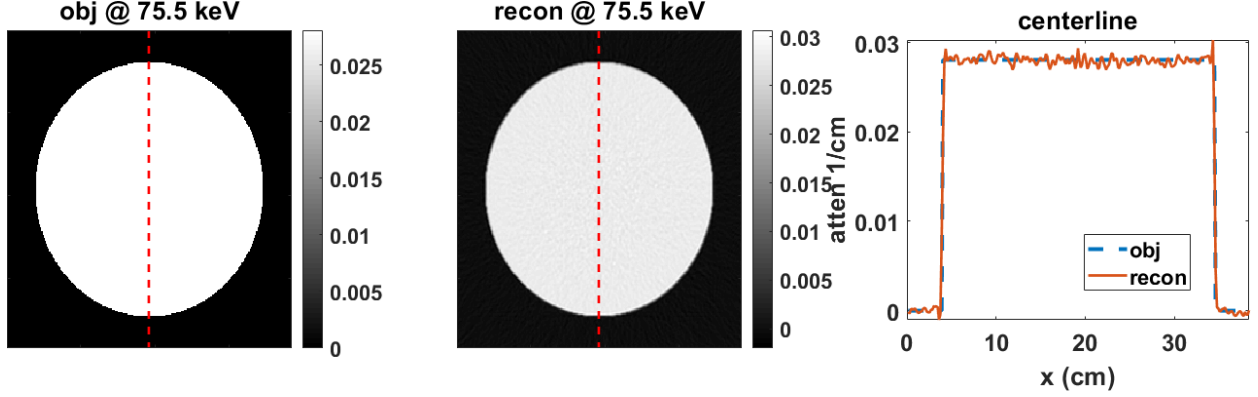


FIG. 6: Reconstruction of the circular phantom. The object $\mu(E, \mathbf{R})$ (left), the reconstruction $\hat{\mu}(E, \mathbf{R})$ (middle) and the center-line plots (right) are all presented at $E = 75.5$ keV.

related to beam hardening.

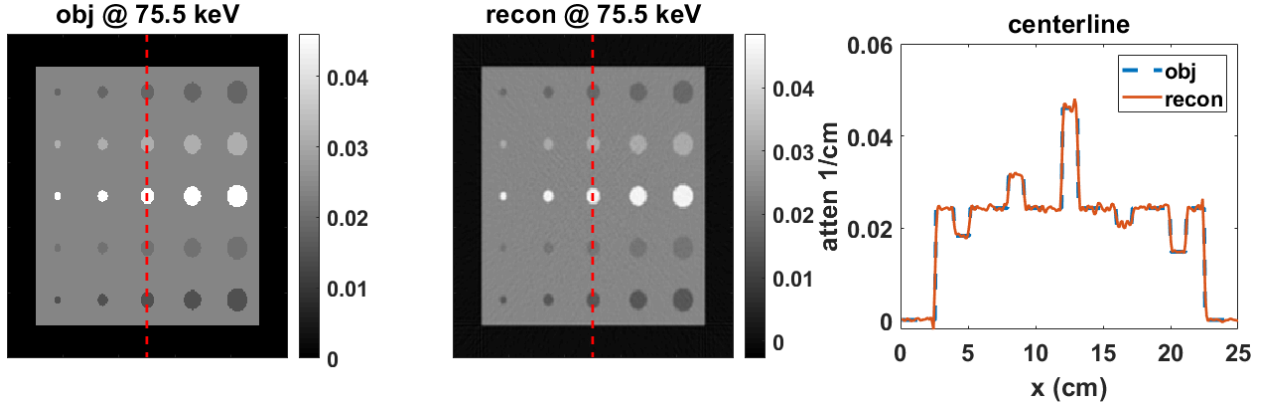


FIG. 7: Reconstruction of the resolution phantom. The object $\mu(E, \mathbf{R})$ (left), the reconstruction $\hat{\mu}(E, \mathbf{R})$ (middle) and the center-line plots (right) are all presented at $E = 75.5$ keV.

230

A second phantom is a multi-material resolution phantom designed with inspiration from Gong et.al.²⁹. The length of the phantom is 20 cm with pixel pitch around 0.1 cm. The phantom, as shown in Figure 7 (left), is a Delrin block with 25 circular inserts in five rows and five columns. In each row, the inserts are made from the same material; in each column, the inserts have the same diameter. From top to bottom, the five materials for the inserts are water, polyvinyl chloride, cast magnesium, acrylic and methanol. The diameter of the inserts are from 0.6 to 1.8 cm with 0.3 cm step. The reconstruction of the resolution phantom are plotted at $E = 75.5$ keV in Figure 7. In the plots, different shade of grey indicate different

materials. The reconstruction results show that the ML estimation algorithm works for a broad range of AM coefficients.

240 Each reconstruction, which calls the ML estimation algorithm 88,200 times, takes approximately 130 seconds on a desktop with a quad-core central processing unit (CPU). The reconstruction can be further sped up using a graphic processing unit (GPU).

VI. DISCUSSION AND FUTURE WORK

Invertibility only requires that the Jacobian $J(\mathbf{A}) \neq 0$ for all coefficients \mathbf{A} . Nonetheless, a smaller $J(\mathbf{A})$ leads to more uncertainty in the estimation as discussed in Section IV. Take the binning detector depicted in Figure 2 (c) as an example, when Bin 1 and Bin 3 do not overlap, the system is invertible for $N = 3$ (when imaging materials with no K-edges). However, the overlap between bins would result in a reduction in the Jacobian and hence more uncertainty in the coefficient estimation. One can employ the CRLB to optimize
 250 bin boundaries for a given set of AM coefficients \mathbf{A} . Since the CRLB varies with \mathbf{A} , the optimum bin boundaries depend on the prior distribution of the objects. An optimum energy-weighting strategy that is not object dependent has been proposed by Wang et. al.³⁰. Their strategy is to set the weights $p_m(E)$ same as the attenuation basis functions $f_i(E)$. They have proved that this measurement strategy provided a sufficient statistic to the X-ray spectral flux. Based on Equation (20), we can prove that this strategy is globally invertible, because $\det[F(\mathbf{E})] \det[P(\mathbf{E})] = \{\det[F(\mathbf{E})]\}^2 \geq 0$, for all \mathbf{E} .

Conventional DECT systems reconstruct the effective atomic number (Z_{eff}) and the electron density (ρ)³¹ from two energy-weighted measurements. However, Z_{eff} and ρ do not capture all of the information about material composition measurable from attenuation-
 260 based X-ray systems. Based on principal component analysis (PCA), Bornefalk et. al.³² have suggested that the intrinsic dimensionality of the attenuation profiles of low-Z materials in the XCOM data base is four. There is definitely potential value in collecting ME X-ray data, but the benefits may depend on the task of the imaging system.

We used a set of basis functions that describe photoelectric, Compton scattering and Rayleigh scattering, because we were curious about whether the Rayleigh coefficient is estimable or not. Rayleigh scattering has often been ignored in DE imaging due to its small contribution in the X-ray attenuation profile. Our results have shown that the Rayleigh

component, A_{rs} , is solvable and the uncertainty in its estimation is comparable to that of the photoelectric coefficient. However, we did not study how important A_{rs} is for the task of material discrimination. Other basis functions that are based on materials of interest (such as water and bone) or on PCA³²⁻³⁴ can be used as well. As pointed out by Alvarez et. al.⁸, the choice of a particular basis set does not affect the invertibility. The uncertainty in the estimated attenuation profile should not be affected by the choice of the basis set either.

We presented an ML estimation algorithm to solve the AM coefficients and demonstrated its application in reconstruction with FBP. This is by no means the optimum reconstruction algorithm. Many works have discussed statistical reconstruction methods in DECT^{35,36}. Instead of a two-step process with FBP as in our demonstration, the statistical reconstruction algorithms estimate $\hat{\mathbf{a}}(\mathbf{R})$ from the raw data directly. These algorithms, promising significant reduction in imaging dose, can be readily extended to MECT.

There are limitations in our framework. Firstly, the physical process considered by the mapping $\mathcal{X} : \mathbf{A} \rightarrow \mathbf{I}$ includes only the attenuation of the X-ray photons, which follows Beer's law, but not signals due to scattered radiation or background radiation. Although scattered radiation and background radiation can be significantly mitigated through anti-scatter grids³⁷, those signals may still affect the invertibility of an realistic system. Secondly, effects that limit detector performance, such as charge sharing^{38,39}, charge trapping^{39,40} and pulse pileup, are ignored. Such details should be considered in the system model when the framework is applied to a specific imaging system.

Another limitation is that, in the derivation of the CRB bound, we assumed the measurement data follow Poisson distribution. For many realistic detectors, the Poisson model is not an accurate model for the measurement data. For example, the energy-weighting functions of a CIX-PC/EI/MI detector introduce correlations between different measurements; and the data collected by a PC detector also have correlations partially due to pulse pileup. Furthermore, electronic noise and nonlinearities may also affect the statistics of the data. Finding the optimum statistical model to describe measurement data for a specific detector is an interesting avenue for future work.

VII. CONCLUSION

We have provided a sufficient condition for the global invertibility of an ME X-ray transform for attenuation-based X-ray imaging. The ME X-ray transform is defined as the mapping from N ($N \geq 2$) AM coefficients to N energy-weighted noise-free measurements. The invertibility of this transform depends greatly on the weighting schemes used in the measurements. Considering scenes with no K-edge materials, we represented the X-ray attenuation profiles with $N = 3$ AM coefficients and proved the global invertibility of the transform for four commonly used weighting schemes. The same framework can be used to check the invertibility of an arbitrary ME X-ray system, such as a system with non-ideal detectors, a system with multiple source emission spectra, and scenes with K-edge materials. This mathematical framework has broad applications in the design of X-ray systems and detectors.

We considered Poisson noise in the measurement data and presented the CRLB on the estimation uncertainty. Furthermore, we presented an ML estimation algorithm and applied the algorithm to estimate AM coefficients for varying lengths of water and varying lengths of iron. The results show that the coefficient corresponding to Rayleigh scattering is estimable. Last but not least, we demonstrated the application of the ML estimator in reconstruction. Two phantoms imaged through a simulated fan-beam CT with ideal three-energy discriminating photon-counting detectors were reconstructed. The reconstructed images match well with the objects and are free of the 'cupping artifacts' induced by beam hardening.

ACKNOWLEDGMENTS

Dr. Clarkson acknowledges the support of NIH R01- EB000803 and P41- EB002035.

DISCLOSURES

The authors declare that there are no conflicts of interest related to this article.

Appendix A: The signs of $\det[F(\mathbf{E})]$ and $\det[D(\mathbf{E})]$

In this appendix, we study the signs of functions $\det[F(\mathbf{E})]$ and $\det[D(\mathbf{E})]$ in S_{123} , where $E_1 < E_2 < E_3$. We first prove the negativity of $\det[F(\mathbf{E})]$ for photoelectric/Compton/Rayleigh

basis functions in S_{123} . Then we prove $\det[D(\mathbf{E})]$ of four special types of detectors is always positive/negative for any \mathbf{E} in space S_{123} , where 'positive' and 'negative' both include zero.

1. The sign of $\det[F(\mathbf{E})]$ for pe/cs/rs basis

Now consider the scenario with no K-edge materials, where three basis functions are sufficient to describe the attenuation profile of any material. Define E_1 as any energy in measurement one, E_2 as any energy in measurement two and E_3 as any energy in measurement three. In the next few paragraphs, we will prove that $\det[F(\mathbf{E})] < 0$ in the subspace S_{123} . As mentioned in the main text, S_{123} is the subspace within the support of the measurements S with property $E_1 < E_2 < E_3$.

To simplify notation, we denote functions

$$\begin{aligned} g(E) &= \frac{f_2(E)}{f_1(E)}; \\ h(E) &= \frac{f_3(E)}{f_1(E)}; \end{aligned} \tag{A1}$$

and matrix

$$G = \begin{bmatrix} 1 & g(E_1) & h(E_1) \\ 1 & g(E_2) & h(E_2) \\ 1 & g(E_3) & h(E_3) \end{bmatrix} \tag{A2}$$

With these notations, we can write the determinant of $F(\mathbf{E})$ as

$$\det[F(\mathbf{E})] = f_1(E_1)f_1(E_2)f_1(E_3) \det G \tag{A3}$$

Now consider $\det G$ as a function of E , where $E = E_1$.

$$\det G(E) = g(E)(h_2 - h_3) + h(E)(g_3 - g_2) + (g_2h_3 - h_2g_3), \tag{A4}$$

where the subscript 2 and 3 represent the function evaluated at E_2 and E_3 , respectively. Since $\det G(E_2) = \det G(E_3) = 0$, the sign of $\det G(E)$ when $E < E_2 < E_3$ can be determined from the derivative $[\det G(E)]'$:

$$\begin{aligned} [\det(G)(E)]' &= g'(E)(h_2 - h_3) + h'(E)(g_3 - g_2) \\ &= h'(E)(h_3 - h_2) \left(-\frac{g'(E)}{h'(E)} + \frac{g_3 - g_2}{h_3 - h_2} \right) \end{aligned} \tag{A5}$$

Based on the X-ray cross section function given in Equation (2) in the main text, we know the following:

- (a). $f_1(E) > 0$, for all $E \in (0, 200)$ keV;
- (b). $h'(E) > 0$;
- (c). The function $g(h)$ is strictly convex for all $E \in (0, 200)$ keV.

The first two conditions, which are the positivity of $f_1(E)$ and the monotonicity of $h(E)$, are obvious based on the function forms of $f_i(E)$ provided in the main text of this paper. The convexity of the function $g(h)$ can be derived from the positivity of its second derivative. Plots of $g(h)$ and its second derivative are shown in Figure 8.

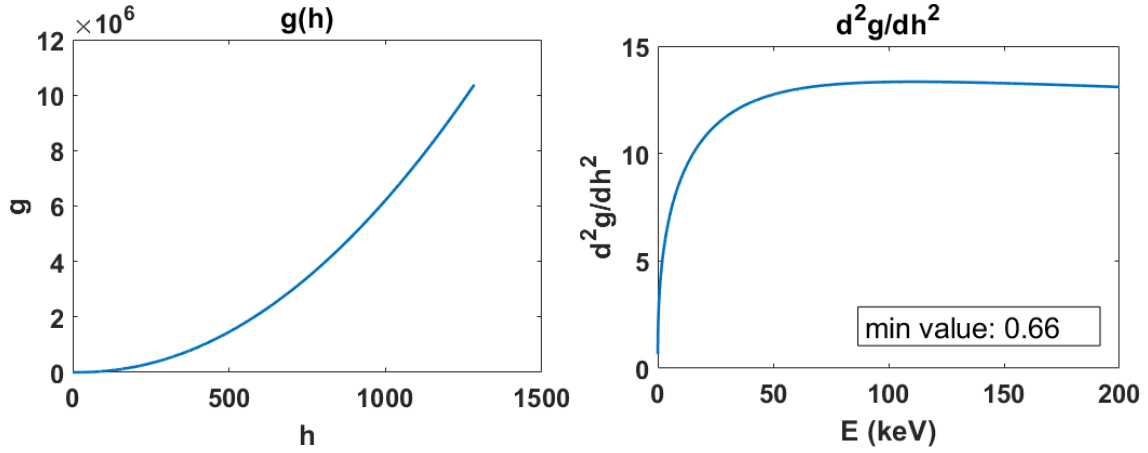


FIG. 8: Plot of function $g(h)$ (left) and d^2g/dh^2 as a function of energy E (right). Within the range of energy that is normally used for imaging, which is $E \in (0, 200)$ keV, d^2g/dh^2 is always positive and hence $g(h)$ is strictly convex for all $E \in (0, 200)$ keV.

340

The following results can be derived from the above properties:

- (a). The signs of the two determinants $\det[F(\mathbf{E})]$ and $\det G$ are the same, since $f_1(E) > 0$ for all $E \in (0, 200)$ keV.
- (b). Due to the monotonicity of $h(E)$, $h'(E)(h_3 - h_2) > 0$.
- (c). The strict convexity of $g(h)$ gives us $\left(-\frac{g'(E)}{h'(E)} + \frac{g_3 - g_2}{h_3 - h_2}\right) \geq \left(-\frac{g'(E_2)}{h'(E_2)} + \frac{g_3 - g_2}{h_3 - h_2}\right) > 0$.

Combining the two facts: $\det(G)(E_2) = 0$ and $[\det(G)(E)]' > 0$ for $0 < E < E_2$, one can derive that $\det(G)(E) < 0$ for $0 < E < E_2 < E_3$. Therefore, $\det[F(\mathbf{E})] < 0$ when $E_1 < E_2 < E_3$.

350 **2. The sign of $\det[D(\mathbf{E})]$ for CIX-PC/EI/MI detectors**

In this section, we consider a counting and integrating X-ray (CIX) detector that measures the photon counts, integrated energy and integrated momentum described by:

$$D_m(E) \propto \begin{cases} 1, & m = 1; \\ E, & m = 2; \\ \sqrt{E}, & m = 3. \end{cases} \quad (\text{A6})$$

The matrix $D(\mathbf{E})$ is

$$D(\mathbf{E}) \propto \begin{bmatrix} 1 & E_1 & \sqrt{E_1} \\ 1 & E_2 & \sqrt{E_2} \\ 1 & E_3 & \sqrt{E_3} \end{bmatrix}. \quad (\text{A7})$$

The matrix $D(\mathbf{E})$ is equivalent to the matrix G defined in the previous section, if $g(E) = E$ and $h(E) = \sqrt{E}$. Following the same derivation in the previous section, since (1) $h(E) = \sqrt{E}$ is monotonically increasing with E , and (2) the function $g(h) = h^2$ is strictly convex for all $E > 0$, we have $\det[D(\mathbf{E})] < 0$ when $E_1 < E_2 < E_3$.

3. The sign of $\det[D(\mathbf{E})]$ for a three-bin detector with non-overlapping bins

In this section, we consider the sign of $\det[D(\mathbf{E})]$ when the energy response function of each bin $D_m(E)$ do not overlap. Since $D_m(E) \geq 0$, the function $D_1(E_1)D_2(E_2)D_3(E_3) \geq 0$ for all $\mathbf{E} \in S$. The other five terms of $\det[D(\mathbf{E})]$, including $D_1(E_1)D_2(E_3)D_3(E_2)$, $D_1(E_2)D_2(E_1)D_3(E_3)$, $D_1(E_3)D_2(E_2)D_3(E_1)$, $D_1(E_2)D_2(E_3)D_3(E_1)$ and $D_1(E_3)D_2(E_1)D_3(E_2)$,
360 are all zero for $\mathbf{E} \in S_{123}$. Therefore, $\det[D(\mathbf{E})] \geq 0$ for all $\mathbf{E} \in S_{123}$.

4. The sign of $\det[D(\mathbf{E})]$ for a three-bin detector with *rect* response functions

In this section, we consider the sign of $\det[D(\mathbf{E})]$ when the energy response function of each bin $D_m(E)$ can be approximated as a *rect* function:

$$D_m(E) = \begin{cases} d_m, & \text{if } l_m \leq E < u_m; \\ 0, & \text{otherwise;} \end{cases} \quad (\text{A8})$$

where l_m and u_m are the lower edge and upper edge of the m^{th} bin. Furthermore, we only consider detectors with bin boundaries satisfying $u_1 < u_2 < u_3$ and $l_1 < l_2 < l_3$.

When there is no overlap between any two bins, $\det[D(\mathbf{E})] = D_1(E_1)D_2(E_2)D_3(E_3) > 0$ in domain S_{123} . When there is overlap between bins, the sign of $\det[D(\mathbf{E})]$ is not obvious. We first consider the determinant of two measurements $J_{m_1 m_2} = D_{m_1}(E_1)D_{m_2}(E_2) - D_{m_2}(E_1)D_{m_1}(E_2)$, where $m_2 > m_1$. In Figure 9, we plot $J_{m_1 m_2}$ as a function of (E_1, E_2) over the domain $E_2 > E_1 > 0$. In the region $E_2 > E_1 > 0$, $J_{m_1 m_2}$ is not zero only in the region indicated with red color (the red rectangle excluding the overlapping square).

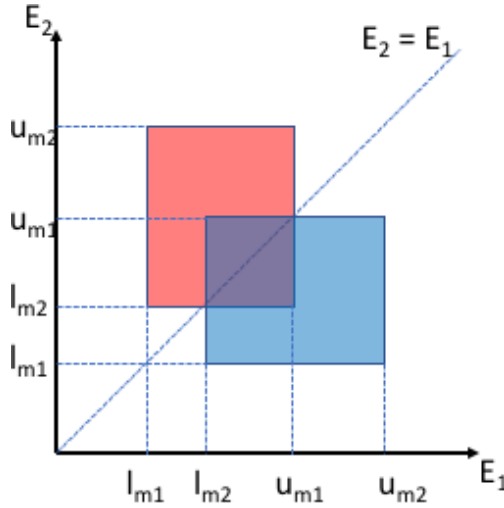


FIG. 9: The determinant of two rect-response detectors $J_{m_1 m_2}$. The red and blue rectangles have values of $d_1 d_2$ and $-d_1 d_2$, respectively. Within the overlapping square and the area outside of the two rectangles, $J_{m_1 m_2}$ is always equals to 0.

370

When all three measurements are considered, $\det[D(\mathbf{E})] = D_1(E_3)J_{23} - D_2(E_3)J_{13} + D_3(E_3)J_{12}$. Note that in the subspace S_{123} , $D_m(E)$, J_{23} , J_{13} and J_{12} are all non-negative, and each term $D_i(E_3)J_{jk}$ has only two values: $d_1 d_2 d_3$ or 0. The determinant $\det[D(\mathbf{E})]$ in S_{123} is negative only when $D_2(E_3)J_{13} > 0$ and $D_1(E_3)J_{23} + D_3(E_3)J_{12} = 0$. The functions J_{12} , J_{23} and J_{13} as functions of (E_1, E_2) are plotted in red (include areas 1, 2, 3 and 4), yellow (include areas 5, 2, 7 and 8) and blue shade (include areas 1, 2, 3, 4, 5, 6, 7 and 8) in Figure 10.

380

The only region for $\det[D(\mathbf{E})]$ to be negative is when $J_{13} > 0$. In Figure 10, the region where $J_{13} > 0$ is indicated by the blue shade, which we further divide into Areas 1–8. In Areas 6–8, $E_3 > E_2 > u_2$ and $\det[D(\mathbf{E})] = D_1(E_3)J_{23} - D_2(E_3)J_{13}$. Since u_2 is the upper

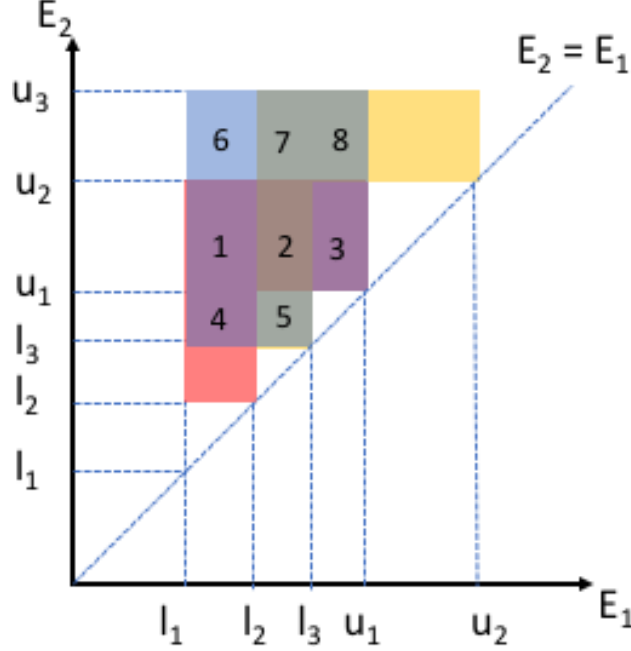


FIG. 10: J_{12} , J_{23} and J_{13} as functions of (E_1, E_2) in region $E_2 > E_1$ are represented in red, yellow and blue shade. $J_{ij} = d_i d_j$ within the area covered by the corresponding color, and $J_{ij} = 0$ otherwise.

boundary of the measurement 2, we know $D_2(E_3) = D_1(E_3) = 0$ and hence $\det[D(\mathbf{E})] = 0$. In Area 1—4, $E_3 > E_2 \geq l_3$ and $\det[D(\mathbf{E})] = -D_2(E_3)J_{13} + D_3(E_3)J_{12}$. Since l_3 is the lower bound of Bin 3, we know $D_3(E_3)/d_3 \geq D_2(E_3)/d_2$ and hence $\det[D(\mathbf{E})] \geq 0$. In Area 5, $E_3 > E_2 \geq l_3 \geq l_2$ and $\det[D(\mathbf{E})] = D_1(E_3)J_{23} - D_2(E_3)J_{13}$. Since l_2 is the lower bound of Bin 2, $D_1(E_3)/d_1 \leq D_2(E_3)/d_2$ and hence $\det[D(\mathbf{E})] \leq 0$. More specifically, when $u_1 < E_3 < u_2$, $\det[D(\mathbf{E})] < 0$ in Area 5. Therefore, $\det[D(\mathbf{E})] < 0$ in the cube defined by $l_2 < E_1 < l_3$, $l_3 < E_2 < u_1$ and $u_1 < E_3 < u_2$; and $\det[D(\mathbf{E})] \geq 0$ otherwise. Note that

390 when $l_3 < u_1$, Area 5 does not exist and $\det[D(\mathbf{E})] \geq 0$ for any \mathbf{E} in S_{123} . In other words, $\det[D(\mathbf{E})]$ is always non-negative in domain S_{123} for an ideal binning detector satisfying the follow three conditions: (1) there is no overlap between Bin 1 and Bin 3, (2) upper boundaries of the bins $u_1 < u_2 < u_3$, and (3) lower boundaries of the bins $l_1 < l_2 < l_3$.

5. The sign of $\det[D(\mathbf{E})]$ for a three-bin detectors with non-ideal energy responses

Photon-counting detectors often have non-overlapping energy thresholds, but the energy resolution may limit the detector's performance. Denote the probability density function (PDF) of the measured energy E' for an incoming photon with energy E , $\text{pr}(E'|E)$, the detector response function of Bin m to a photon with energy E can be expressed as:

$$D_m(E) = \int_{t_m}^{t_{m+1}} dE' d_m(E) \text{pr}(E'|E), \quad (\text{A9})$$

where $d_m(E)$ is the sensitivity of the m^{th} bin to an incoming photon with energy E , t_m and t_{m+1} are the lower and upper threshold of the m^{th} bin, respectively. For ideal detector, $\text{pr}(E'|E)$ is a Dirac-delta function and the sensitivity $d_m(E)$ is a constant d_m . Therefore, the detector response functions are *rect* functions as described in the previous section. For non-ideal detectors, the finite energy resolution introduced by $\text{pr}(E'|E)$ produces blurred boundary to the detector response functions $D_m(E)$. For example, the energy response functions of a non-ideal three-bin detector are shown in Figure 11.

Consider the detector sensitivity function $d_m(E)$ as a constant. For many photon-counting binning detectors with good energy resolution, the energy response function $\text{pr}(E'|E)$ is narrow and can be considered as a truncated function (e.g. truncated Gaussian or triangle function). In such cases, the detector response functions can be approximated by step-wise functions. These step-wise functions are flat between the two bin boundaries t_m and t_{m+1} , monotonically decrease as the energy E gets further away from the bin boundaries, and are zero beyond the bin boundaries of the neighboring bins. Mathematically, we describe the response functions of such a detector with:

$$\begin{cases} D_m(E) = 0, & \text{when } E < t_{m-1}; \\ D_m(E_1) \leq D_m(E_2), & \text{when } E_1 < E_2 < t_m; \\ D_m(E_1) = D_m(E_2) = d_m, & \text{when } t_m < E_1 < E_2 < t_{m+1}; \\ D_m(E_1) \geq D_m(E_2), & \text{when } t_{m+1} < E_1 < E_2; \\ D_m(E) = 0, & \text{when } E > t_{m+2}. \end{cases} \quad (\text{A10})$$

Denote the order of Bin 1, Bin 2 and Bin 3 such that $t_1 < t_2 < t_3$.

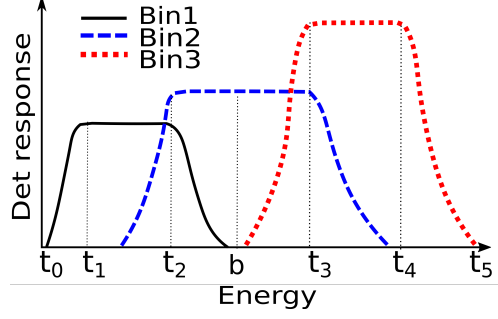


FIG. 11: The detector response function of a three-bin non-ideal energy-discriminating detector.

With these response functions, the determinant of two measurements satisfy the following inequality:

$$\begin{aligned}
 J_{12} &= D_1(E_1)D_2(E_2) - D_2(E_1)D_1(E_2) \\
 &\geq \begin{cases} D_1(E_1)D_2(E_2) \geq 0, & \text{when } E_2 > t_3; \\ D_1(E_1)D_2(E_2) - D_2(E_1)D_1(E_1) = 0, & \text{when } t_2 < E_1 < E_2 < t_3; \\ D_1(E_1)D_2(E_2) - d_1d_2 = 0, & \text{when } t_1 < E_1 < t_2 < E_2 < t_3; \\ D_1(E_1)D_2(E_2) - D_2(E_2)D_1(E_2) = 0, & \text{when } t_1 < E_1 < E_2 < t_2; \\ D_1(E_1)D_2(E_2) \geq 0, & \text{when } E_1 < t_1. \end{cases} \quad (\text{A11})
 \end{aligned}$$

Therefore, $J_{12} \geq 0$ in the region $E_2 > E_1$.

Now we focus on the scenario that detector response functions of the first bin and the third bin do not overlap. In other words, there exists a constant value b such that when $E > b$, $D_1(E) = 0$ and $D_3(E) \geq 0$; and when $E < b$, $D_1(E) \geq 0$ and $D_3(E) = 0$. This scenario is possible when the size of the blur introduced by the finite energy resolution is small compared to the width of Bin 2. When there is no overlap between Bin 1 and Bin 3,

$$D_3(E_i)D_1(E_j) = 0 \quad \text{when } E_i < E_j. \quad (\text{A12})$$

Denote a step function as

$$\text{step}(E, b) = \begin{cases} 0, & \text{if } E < b; \\ 1, & \text{if } E \geq b; \end{cases} \quad (\text{A13})$$

In the region $E_1 < E_2 < E_3$, the sign of $\det[D(\mathbf{E})]$ can be determined by

$$\begin{aligned}
\det[D(\mathbf{E})] &= D_1(E_1)D_2(E_2)D_3(E_3) + D_1(E_2)D_2(E_3)D_3(E_1) + D_1(E_3)D_2(E_1)D_3(E_2) \\
&\quad - D_1(E_1)D_2(E_3)D_3(E_2) - D_1(E_3)D_2(E_2)D_3(E_1) - D_1(E_2)D_2(E_1)D_3(E_3) \\
&= D_2(E_2)D_1(E_1)D_3(E_3) - D_1(E_1)D_2(E_3)D_3(E_2) - D_1(E_2)D_2(E_1)D_3(E_3) \\
&= \text{step}(E_2, b) [D_2(E_2)D_3(E_3) - D_2(E_3)D_3(E_2)] D_1(E_1) \\
&\quad + [1 - \text{step}(E_2, b)] [D_2(E_2)D_1(E_1) - D_1(E_2)D_2(E_1)] D_3(E_3) \\
&\geq 0,
\end{aligned} \tag{A14}$$

where the first equality stems from Equation (A12) and the inequality has been proved in Equation (A11).

To sum up, photon-counting detectors that satisfy conditions given by Equation (A10) and the condition the Bin 1 and Bin 3 do not overlap have a non-negative $\det[D(\mathbf{E})]$ in the
410 region $E_1 < E_2 < E_3$.

REFERENCES

a) Email: dingy@email.arizona.edu; Author to whom correspondence should be addressed.

b) Email: clarkson@radiology.arizona.edu

c) Email: ashoka@optics.arizona.edu

¹Alvarez Robert E, Macovski Albert. Energy-selective reconstructions in X-ray computerised tomography *Physics in Medicine & Biology*. 1976;21:733.

²Lehmann LA, Alvarez RE, Macovski Aetal, et al. Generalized image combinations in dual kVp digital radiography *Medical Physics*. 1981;8:659–667.

³Barnes Gary T, Sones Richard A, Tesic Mike M, Morgan Douglas R, Sanders John N.
420 Detector for dual-energy digital radiography. *Radiology*. 1985;156:537–540.

⁴Cardinal H Neale, Fenster Aaron. Theoretical optimization of a split septaless Xenon ionization detector for dual-energy chest radiography *Medical Physics*. 1988;15:167–180.

⁵Roessl E, Proksa R. K-edge imaging in X-ray computed tomography using multi-bin photon counting detectors *Physics in Medicine & Biology*. 2007;52:4679.

- ⁶Fredenberg Erik. Spectral and dual-energy X-ray imaging for medical applications *Nuclear Instruments and Methods in Physics Research Section A: Accelerators, Spectrometers, Detectors and Associated Equipment*. 2018;878:74–87.
- ⁷Levine Zachary H. Nonuniqueness in dual-energy CT *Medical Physics*. 2017;44:e202–e206.
- ⁸Alvarez Robert E. Invertibility of the dual energy X-ray data transform *Medical Physics*. 2019;46:93–103.
- ⁹Sukovle P, Clinthorne NH. Basis material decomposition using triple-energy X-ray computed tomography in *IMTC/99. Proceedings of the 16th IEEE Instrumentation and Measurement Technology Conference (Cat. No. 99CH36309)*;3:1615–1618IEEE 1999.
- ¹⁰Lehmann L, Alvarez R, Macovski A, et al. Energy-selective reconstructions in X-ray computerized tomography *Medical Physics*. 1981;8:659–667.
- ¹¹Macovski A, Alvarez RE, Chan JL-H, Stonestrom JP, Zatz LM. Energy dependent reconstruction in X-ray computerized tomography *Computers in Biology and Medicine*. 1976;6:325–336.
- ¹²Tapiovaara Markku J, Wagner R. SNR and DQE analysis of broad spectrum X-ray imaging *Physics in Medicine & Biology*. 1985;30:519.
- ¹³Flohr Thomas G, McCollough Cynthia H, Bruder Herbert, et al. First performance evaluation of a dual-source CT (DSCT) system *European Radiology*. 2006;16:256–268.
- ¹⁴Zhang Da, Li Xinhua, Liu Bob. Objective characterization of GE discovery CT750 HD scanner: gemstone spectral imaging mode *Medical Physics*. 2011;38:1178–1188.
- ¹⁵Altman A, Carmi R. TU-E-210A-03: a double-layer detector, dual-energy CT—principles, advantages and applications *Medical Physics*. 2009;36:2750–2750.
- ¹⁶Kraft Edgar, Fischer Peter, Karagounis Michael, et al. Counting and integrating readout for direct conversion X-ray imaging: Concept, realization and first prototype measurements *IEEE Transactions on Nuclear Science*. 2007;54:383–390.
- ¹⁷Karg J, Niederlöhner D, Giersch J, Anton G. Using the Medipix2 detector for energy weighting *Nuclear Instruments and Methods in Physics Research Section A: Accelerators, Spectrometers, Detectors and Associated Equipment*. 2005;546:306–311.
- ¹⁸Taguchi Katsuyuki, Iwanczyk Jan S. Vision 20/20: Single photon counting X-ray detectors in medical imaging *Medical Physics*. 2013;40.
- ¹⁹Fulks Watson. *Advanced calculus: an introduction to analysis*. John Wiley & Sons 1978.
- ²⁰Williamson Jeffrey F, Li Sicong, Devic Slobodan, Whiting Bruce R, Lerma Fritz A. On

two-parameter models of photon cross sections: Application to dual-energy CT imaging
Medical Physics. 2006;33:4115–4129.

²¹Trubey D. K.. *HUGI VI notes documentation for the DLC-146 code package*. Radiaton
460 Safety Information Computational Center 1989.

²²Berger MJ, Hubbell JH, Seltzer SM, et al. XCOM: Photon Cross
Sections Database. NIST Standard Reference Database 8 (XGAM)
<http://physics.nist.gov/PhysRefData/Xcom/Text/XCOM.html>. 1998.

²³Krantz Steven G, Parks Harold R. *The implicit function theorem: history, theory, and
applications*. Springer Science & Business Media 2012.

²⁴Cramer Harald. *Mathematical methods of statistics* . 1946.

²⁵Rao C Radhakrishna. Information and the accuracy attainable in the estimation of statis-
tical parameters *Bulletin of the Calcutta Mathematical Society*. 1945;37:81–89.

²⁶Boyd Stephen, Boyd Stephen P, Vandenberghe Lieven. *Convex optimization*. Cambridge
470 university press 2004.

²⁷Nocedal Jorge, Wright Stephen. *Numerical optimization*. Springer Science & Business
Media 2006.

²⁸Ding Yijun, Ashok Amit. X-ray measurement model and information-theoretic metric in-
corporating material variability with energy correlations in *Anomaly Detection and Imag-
ing with X-rays (ADIX) IV*;10999:109990JInternational Society for Optics and Photonics
2019.

²⁹Gong Qian, Stoian Razvan-Ionut, Coccarelli David S, Greenberg Joel A, Vera Esteban,
Gehm Michael E. Rapid simulation of X-ray transmission imaging for baggage inspection
via GPU-based ray-tracing *Nuclear Instruments and Methods in Physics Research Section
480 B: Beam Interactions with Materials and Atoms*. 2018;415:100–109.

³⁰Wang Adam S, Pelc Norbert J. Sufficient statistics as a generalization of binning in spectral
X-ray imaging *IEEE transactions on medical imaging*. 2010;30:84–93.

³¹Martz Harry E, Seetho Issac M, Champley Kyle E, Smith Jerel A, Azevedo Stephen G.
CT dual-energy decomposition into X-ray signatures ρ_e and Z_e in *Anomaly Detection and
Imaging with X-Rays (ADIX)*;9847:98470DInternational Society for Optics and Photonics
2016.

³²Bornefalk Hans. XCOM intrinsic dimensionality for low-Z elements at diagnostic energies
Medical Physics. 2012;39:654–657.

- ³³Alvarez Robert E. Dimensionality and noise in energy selective X-ray imaging *Medical Physics*. 2013;40:111909.
- ³⁴Weaver John B, Huddleston Alan L. Attenuation coefficients of body tissues using principal-components analysis *Medical Physics*. 1985;12:40–45.
- ³⁵Xu Jingyan, Frey Eric C, Taguchi Katsuyuki, Tsui Benjamin MW. A Poisson likelihood iterative reconstruction algorithm for material decomposition in CT in *Medical Imaging 2007: Physics of Medical Imaging*;6510:65101ZInternational Society for Optics and Photonics 2007.
- ³⁶Fessler Jeffrey A, Elbakri Idris A, Sukovic Predrag, Clinthorne Neal H. Maximum-likelihood dual-energy tomographic image reconstruction in *Medical Imaging 2002: Image Processing*;4684:38–49International Society for Optics and Photonics 2002.
- ³⁷Tang C-M, Stier E, Fischer K, Guckel H. Anti-scattering X-ray grid *Microsystem Technologies*. 1998;4:187–192.
- ³⁸Shikhaliev Polad M, Fritz Shannon G, Chapman John W. Photon counting multienergy X-ray imaging: Effect of the characteristic X rays on detector performance *Medical Physics*. 2009;36:5107–5119.
- ³⁹Xu Cheng, Danielsson Mats, Bornefalk Hans. Evaluation of energy loss and charge sharing in cadmium telluride detectors for photon-counting computed tomography *IEEE Transactions on Nuclear Science*. 2011;58:614–625.
- ⁴⁰Knoll Glenn F. *Radiation detection and measurement*. John Wiley & Sons 2010.